

Quantum transport regimes in quartic dispersion materials with Anderson disorder

Mustafa Polat,¹ Hazan Özkan,² and Haldun Sevincli^{1,*}

¹*İzmir Institute of Technology, Department of Materials Science and Engineering, 35430 Urla, İzmir, Turkey*

²*İzmir Institute of Technology, Department of Photonics, 35430 Urla, İzmir, Turkey*

Mexican-hat-shaped quartic dispersion manifests itself in certain families of single-layer two-dimensional hexagonal crystals such as compounds of groups III-VI and groups IV-V as well as elemental crystals of group V. Quartic band forms the valence band edge in various of these structures, and some of the experimentally confirmed structures are GaS, GaSe, InSe, SnSb and blue phosphorene. Here, we numerically investigate strictly-one-dimensional (1D) and quasi-one dimensional (Q1D) nanoribbons with quartic dispersion and systematically study the effects of Anderson disorder on their transport properties with the help of a minimal tight-binding model and Landauer formalism. We compare the analytical expression for the scaling function with simulation data to deduce about the domains of diffusion and localization regimes. In 1D, it is shown that conductance drops dramatically at the quartic band edge compared to a quadratic band. As for the Q1D nanoribbons, a set of singularities emerge close to the band edge, which suppress conductance and lead to short mean-free-paths and localization lengths. Interestingly, wider nanoribbons can have shorter mean-free-paths because of denser singularities. However, the localization lengths do not necessarily follow the same trend. The results display the peculiar effects of quartic dispersion on transport in disordered systems.

I. INTRODUCTION

Several families of two-dimensional (2D) materials have been identified since the first isolation of a graphene monolayer, and they have received considerable attention due to their unusual and unique properties. They are not only interesting for fundamental science, but are also promising candidates for next-generation devices [1–12]. Many of the novel properties are related to their electronic band structures some of which are unprecedented. Mexican hat shaped (MHS) quartic energy dispersion is one of them. Graphene like honeycomb lattices of group V elements, group III-VI and group IV-V compounds in hexagonal $P\bar{6}m2$ symmetry display MHS quartic dispersion in their valance bands (VB). In some of these structures, the valence band maximum is formed by the MHS quartic band. [13–46]. Owing to their unusual band structure, these materials are reported to have peculiar magnetic and ferroelectric phases, very high thermoelectric efficiencies and potential to be useful for applications like water splitting, optoelectronics, photonics, thermoelectrics [21, 30–36, 45, 47–51]. On the experimental side, single and few layers of quartic materials such as gallium based compounds (GaS, GaSe, GaTe) [52–57], InSe [58–60] blue phosphorene [61], and SnSb [62] have been synthesized and their distinctive properties have been reported.

A key feature in the electronic structure of MHS quartic dispersion is the strong (inverse-square-root) van Hove singularity with divergent DOS at the VB edge. Such strong singularity and divergent DOS is uncommon in 2D. In addition to the strong singularity,

the pristine transmission spectrum displays a step-like behavior at the band edge. Stepwise transmission spectrum is a characteristic feature of 1D systems and in 2D it is observed only in quartic materials. These peculiarities of quartic dispersion, together with finite amounts of disorder are potentially responsible for strong scatterings that could alter the electronic properties significantly. The effects of disorder on the transport properties of quartic materials have not been addressed in the literature before. Here, using nonequilibrium Green's function (NEGF) methodology, we study quantum transport properties around the quartic VB edge. We consider large-scale quartic systems by taking advantage of a minimal tight-binding (TB) model suggested in Ref.[21] and thus we are able to determine the transport length scales of these systems in the presence of Anderson disorder. The effects of Anderson disorder on conductance (G) are numerically investigated in the case of strictly-one-dimensional (1D) and quasi-one dimensional (Q1D) systems at the weak disorder limit. Our results show that there is a dramatic suppression of transmission at the quartic band edge, which can not be understood using the conventional effective mass approaches or any multiple band models.

The rest of this paper is organized as follows. In Sec. II, the computational models of interest are introduced. The effects of disorder on G are separately discussed in Sec. III for both 1D and Q1D systems. Sec. IV summarizes our conclusions.

II. SYSTEMS AND METHODS

For two-dimensional hexagonal lattices of group-V elements, it was previously shown that a second nearest neighbor TB approximation is suitable to study the

* Corresponding author: haldunsevincli@iyte.edu.tr

quartic dispersion [21],

$$H = -t_1 \sum_{\langle ij \rangle} (c_i^\dagger c_j + \text{H.c.}) - t_2 \sum_{\langle\langle ij \rangle\rangle} (c_i^\dagger c_j + \text{H.c.}), \quad (1)$$

where $c_i(c_i^\dagger)$ annihilates (creates) an electron at lattice site i , t_1 and t_2 are the first and the second nearest neighbor hopping parameters, respectively, and accordingly the summations run over the first and the second nearest neighbors.

The solution of above Hamiltonian is familiar from graphene band structure [63], which can be expressed as $E_{\pm}(\mathbf{k}) = \pm t_1 \sqrt{3 + f(\mathbf{k})} - t_2 f(\mathbf{k})$, with $f(\mathbf{k}) = 2 \cos(\sqrt{3}k_y a) + 4 \cos(\sqrt{3}k_y a/2) \cos(3k_x a/2)$, \mathbf{k} and a being the wave vector and the lattice constant. Different from the half-filled bands of π -orbitals of graphene, we are interested in completely filled bands (eg. replacing carbon with nitrogen, see Ref. [21]). In this sense, valance band maximum (VBM) is set to that of the highest occupied electronic state by assuming two electrons per atom in this study. For $\xi = t_2/t_1 > 1/6$, the above dispersion yields a quartic band around the VB edge, such that

$$E \propto (k^2 - k_c^2)^2. \quad (2)$$

We choose the TB parameters to reproduce the topmost VB of hexagonal nitrogen, because it is well separated from the rest of the bands [16, 21, 27]. That is, $t_1=6.1$ eV and $t_2=1.27$ eV are chosen, which corresponds to $\xi = 0.21$. In Fig. 1(a), the quartic band for nitrogen as obtained from our TB approximation is shown to have perfect agreement with that obtained from density functional theory (DFT) calculations, especially for low energy holes [21]. For the sake of simplicity, we refer the energy values ranging from the minimum of the Mexican hat at the center of the BZ to its maximum, namely the VBM, as the MHS energy region. This is not meant to exclude the energies close to these values from being quartic in dispersion, but to emphasize that in this energy range there are four solutions at a given direction in k -space for the 2D structure. In the case of hexagonal nitrogen, the MHS energy region lies within $-0.47 \text{ eV} < E - E_{\text{VBM}} < 0$.

In this study, starting from a toy model, namely monatomic chain, we investigate the electronic and transport properties of the Q1D nitrogen nanoribbons (NRs) with zigzag and armchair edges (ZNR and ANR) in the presence of uncorrelated disorders. The hexagonal lattice structure and the unit cells of these Q1D systems are illustrated in Fig. 1(b). The puckered geometry of the lattice does not play a role for the purposes of this study therefore it is disregarded. As for short-range disorder, Anderson disorder is introduced by adding the term $H_A = \sum_i \epsilon_i c_i^\dagger c_i$ to the Hamiltonian. Here, ϵ_i represents the on-site energy, which randomly fluctuates in the energy interval $[-W/2, W/2]$ with a fixed disorder strength $W = 25$ meV and $W = 250$ meV for the chain and

ribbon geometries, respectively. The overall contribution of the on-site potential energies is set to zero, that is $\sum_i \epsilon_i = 0$. In all cases, Eq. 1 with additional on-site terms is numerically solved for various system lengths, L .

Conductance values are computed within the Landauer approach using NEGF formalism, further details of which can be found elsewhere [64, 65]. The system is partitioned as left, center and right (L , C , and R) regions, where L/R have semi-infinite geometry and are made-up of pristine material to stand for the electrodes. The self energies due to coupling to the electrodes are computed using the surface Green's functions [66]. Scattering events are allowed to take place only in the C region for which the retarded Green function can be expressed as $\mathcal{G}_{CC}^r(E) = [(E + i0^+)I - H_{CC} - \Sigma_L^r - \Sigma_R^r]^{-1}$, with 0^+ being an infinitesimal positive number, I the identity matrix, H_{CC} is Hamiltonian of the C region, $\Sigma_{L/R}^r = H_{CL/CR} \mathcal{G}_{LL/RR}^{r,0} H_{LC/RC}$ are the self-energy

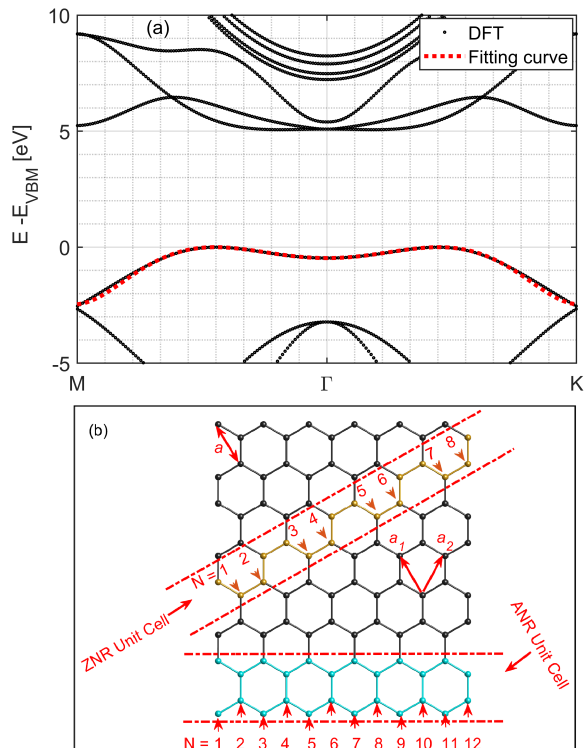


FIG. 1. (a) shows the fitting curve (red dots) of the topmost VB of DFT (black circles), which is defined by a ring of radius $k_0 \approx 0.78 \text{ \AA}$ and a well of $E_0 \approx 0.47$ eV deep at the Γ -point. The bandwidth of the upper VB nearly equals to 2.6 eV. (b) illustrates the top view of hexagonal lattice structure in which the unit cells, the lattice constant a , the basis vectors $a_1 = a(\sqrt{3}/2, 1/2)$ and $a_2 = a(\sqrt{3}/2, -1/2)$ are depicted. The widths of the NRs denoted by the number of N are separately shown for a ZNR with $N = 8$ and an ANR with $N = 12$. The device lengths are taken as $L = Ma$ for a ZNR and $L = Ma\sqrt{3}$ for an ANR, respectively, where M is the number of unit cell in the Q1D system.

matrices with the free Green's functions $\mathcal{G}_{LL/RR}^{r,0} = [(E + i0^+)I - H_{LL/RR}]^{-1}$ of the isolated L and R reservoirs. The level-broadening caused by system-electrode coupling is $\Gamma_{L/R} = i(\Sigma_{L/R} - \Sigma_{L/R}^\dagger)$, and the transmission amplitude reads

$$\mathcal{T}(E) = \text{Tr} \left[\mathcal{G}_{CC} \Gamma_L \mathcal{G}_{CC}^\dagger \Gamma_R \right]. \quad (3)$$

At zero temperature, conductance is given by $G(E) = G_o \mathcal{T}(E)$, where $G_o = 2e^2/h$ is the quantum of conductance, and the density of states (DOS) is computed as $\rho(E) = -1/\pi \text{Im}[\text{Tr}[\mathcal{G}^r(E)]]$. System sizes should be large enough for a reliable analysis of the localization regime. In order to be able to simulate large systems a recursion-decimation algorithm is implemented [67]. As for the statistical average of conductance, simple $\langle G \rangle$ averaging over a set of samples may not converge towards any meaningful value, since G does not follow Gaussian statistics in the localized regime [68–71]. Therefore, a logarithmic average $\langle \ln G \rangle$ over 100 samples at each system length L is considered in this study. In this way, statistical average of conductance is obtained via $G_{\text{av}} = \exp(\langle \ln G \rangle)$, which is expected to give a better statistical result [70, 71].

Mean-free path (ℓ_{mfp}) and localization length (ℓ_{loc}) are extracted by fitting simulation data to

$$G_{\text{av}} = \begin{cases} \frac{N_{\text{ch}}}{1 + L/\ell_{\text{mfp}}}, & \text{diffusion} \\ \alpha \exp\left(-\frac{L}{\ell_{\text{loc}}}\right), & \text{localization} \end{cases} \quad (4)$$

where N_{ch} being the number of channels, and α is a fitting parameter. In the diffusion regime, the conductance scales as $G_{\text{av}} \sim 1/L$, obeying Ohm's law. On the other hand, it decays exponentially with L in the Anderson localization regime [72]. Interrelation between transport length scales in 1D systems is set by Thouless relation based on random matrix theory, which conditions that $\ell_{\text{loc}} = (\eta[N_{\text{ch}}-1]+2)/2 \ell_{\text{mfp}}$ [71], where $\eta = 1$ in the absence of external magnetic field, simplifying to

$$\ell_{\text{loc}} = \frac{N_{\text{ch}} + 1}{2} \ell_{\text{mfp}}. \quad (5)$$

Consistency of numerical results are confirmed using Eq. 5.

III. RESULTS

A. Monatomic Chain with Quartic Dispersion

Effects of disorder on the transport characteristics of structures with quartic dispersion have not been addressed in the literature before. Therefore, we first study these systems in their simplest realizations, namely the strictly 1D case. For this purpose, we use a

monatomic chain within the second nearest neighbor empirical TB model. The corresponding dispersion relation is $E(k) = 2t_1 \cos(ka) + 2t_2 \cos(2ka)$, with $k \in [-\pi/a, \pi/a]$. Such a dispersion relation can be expanded around $k=0$ as $E/t_1 \simeq 2(1+\xi) - (ka)^2(1+4\xi) + (ka)^4(1+16\xi)/12$. As a special case, $\xi = -1/4$ leads to a purely quartic dispersion, $E \propto k^4$. For $\xi < -1/4$, a quartic band with MHS emerges (Fig. 2d). In this study, $t_1 = -1$ eV and $t_2 = 1/3$ eV, corresponding to $\xi_{\text{chain}} = -1/3$, are utilized to represent the quartic dispersion, whereas for the quadratic chain $t_1 = -1$ eV and $t_2 = 0$ eV, corresponding to $\xi = 0$, are set (Fig 2a). Band dispersion, density of states (DOS, ρ), and zero temperature ballistic conductance ($G_{\text{ballistic}}$) of the quadratic chain are shown in Fig. 2(a-c), respectively. The corresponding plots for the quartic dispersion are given in Fig. 2(d-f). Both numerical (black) and analytical results (red-dashed) for DOS are shown in Fig. 2(b,e), with

$$\rho(E) = \frac{N_{\text{atom}}}{16\pi t_2 \chi \left(\frac{1}{\sqrt{1-(\gamma+\chi)^2}} + \frac{1}{\sqrt{1-(\gamma-\chi)^2}} \right)}, \quad (6)$$

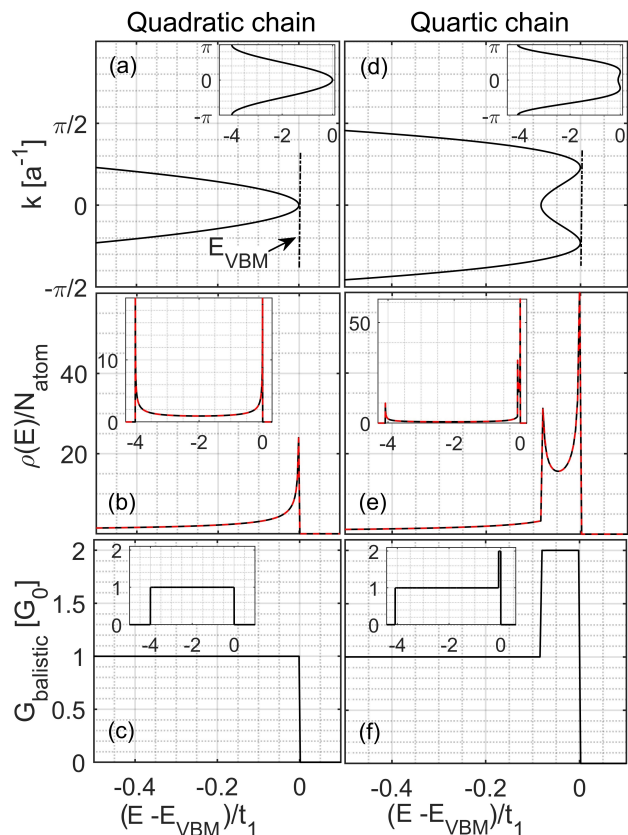


FIG. 2. In the first column, (a) the band structure, (b) DOS per atom, and (c) $G_{\text{ballistic}}$ for the quadratic chain within $(E - E_{\text{VBM}})/t_1 \in [-0.5, 0.1]$ are plotted. The second column shows the same plots for the quartic chain with the same scales as in the first column. The insets in each plot exhibit the full spectra of the chains.

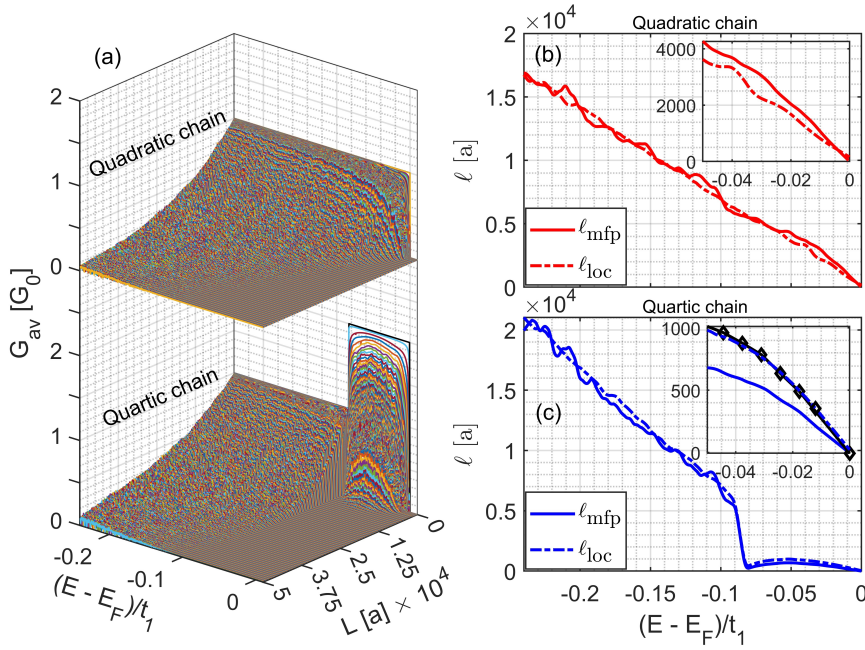


FIG. 3. (a) 3D plot of G_{av} as a function of E and L for quadratic (top panel) and quartic (bottom panel) chains at $W = 25$ meV. l_{mfp} (solid curves) and l_{loc} (dash-dotted curves) are plotted for quadratic chain in (b) and quartic chain in (c). The zoom-ins in each plot show the transport length scales within $(E - E_{VBM})/t_1 \in [-0.05, 0]$. A black solid curve with unfilled diamonds in (c) corresponds to Thouless relation.

for the quartic case, where $\xi < -1/4$, $\varphi = E/4t_2$, $\gamma = 1/4\xi$, and $\chi = -\sqrt{\gamma^2 + \varphi + \frac{1}{2}}$. It is evident that the quartic dispersion gives rise to a much stronger van Hove singularity at E_{VBM} (see Fig. 2) together with an additional singularity at $E - E_{VBM} = t_1(1 + 4\xi)^2/4\xi$. Stepwise $G_{ballistic}$ emerges in both cases, which is the characteristic of 1D systems. $G_{ballistic}$ is doubled for the quartic chain at the MHS energy region, whose width depends on t_1 and t_2 and it is $0.083t_1$ in the present case.

For investigating the effects of disorder, we restrict ourselves to the energies around the VB edge. In the chosen energy interval $(E - E_{VBM})/t_1 \in [-0.25, 0]$, G_{av} are plotted as a function of E and L in Fig. 3(a) for the quadratic (top panel) and quartic (bottom panel) chains. G_{av} is computed for lengths ranging from zero up to $5 \times 10^4 a$. At short distances, G_{av} decreases very fast at the quartic edge and the step exhibits a rounded shape. At energies away from the VBM, conductance decreases relatively slowly, in fact slower than the corresponding energies of the quadratic band. Simulation data of the quadratic and quartic chains are fitted with Eq. 4, and l_{mfp} and l_{loc} are shown in Fig. 3(b) and (c), respectively. It should be noted that the simulation data above $G_{ballistic}/2$ are used for the l_{mfp} fitting processes of both chains, which will be discussed in further detail in Section III C. As it is shown in Fig. 3(b), l_{mfp} and l_{loc} of quadratic chain are equal, in agreement with Thouless relation, i.e., $l_{loc}/l_{mfp} = 1$ for $N_{ch} = 1$. In a similar fashion, l_{mfp} and l_{loc} curves for the quartic chain are displayed in Fig. 3(c). As expected, l_{mfp} of quartic chain equals to l_{loc} except for the quartic edge with $N_{ch} = 2$, where the ratio turns out to be $l_{loc}/l_{mfp} \sim 1.5$ as suggested by Thouless relation. Interestingly, l_{mfp} (l_{loc}) of the quartic chain is approximately six (four) times

smaller than that of the quadratic chain at the quartic edge (see insets of Fig. 3(b) and (c)). We compare transmission of carriers that are inside or outside the MHS energy region. In the MHS energy region with weak disorder ($E = E_{VBM} - 0.05t_1$), and disorder strength is $W = 25$ meV, we have $l_{mfp} = 700a$ and $l_{loc} = 1010a$ (see Fig. 3(c)). In comparison, we compute transmission at $E = E_{VBM} - t_1$ with a much stronger disorder ($W = 250$ meV) and find $l_{mfp} = 1983a$ and $l_{loc} = 1996a$, which are several times larger than those in the MHS energy region with weaker disorder. This comparison in another illustration of the role of strong singularity in transport properties of quartic systems.

B. Nanoribbons with Quartic Dispersion

The electronic and transport properties of the Q1D quartic systems are investigated for ZNR and ANR of nitrogen with the TB parameters of $t_1 = 6.1$ eV and $t_2 = 1.27$ eV. Widths are chosen as $N = 10$, i.e., $N_{atom} = 20$ in a unit cell for both cases. The full spectra of considered bands, $\rho(E)$ per area, and $G_{ballistic}$ as a function of dimensionless energy $(E - E_{VBM})/t_1$ are shown in the upper panels of Fig. 4. Valence band edges of the corresponding spectra are displayed in the lower panels. In the band structure of ZNR, a family of quartic bands appears around the VBM, where some of them exhibit crossings (see the bottom-left of the left panel of Fig. 4). In 2D, the critical wave-vectors that form the band edge are degenerate and nonisolated, which give rise to a strong van Hove singularity. In Q1D NRs, the critical wave-vectors are isolated and nondegenerate, whereas van Hove singularities are still strong because of the reduced dimension. In addition, there exist numerous

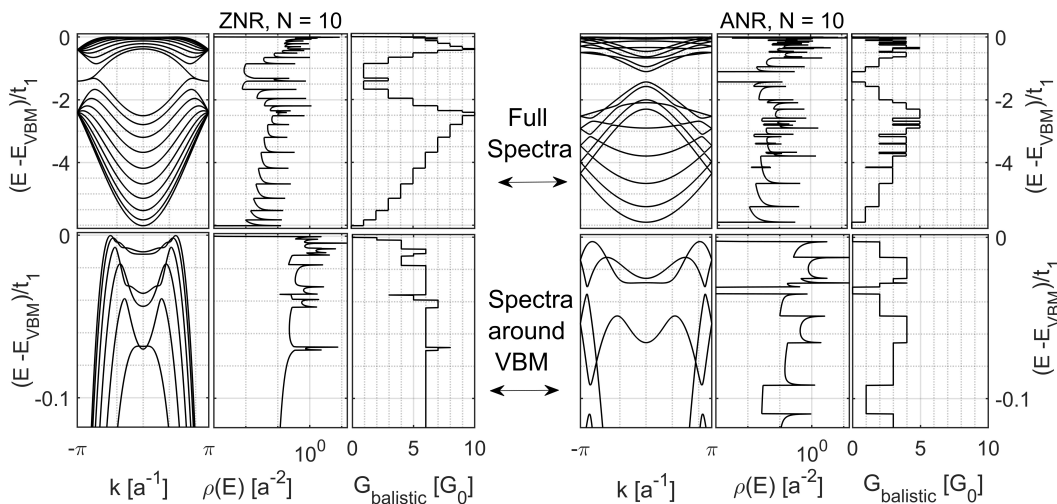


FIG. 4. Energy band structure, density of states and pristine conductance for ZNR (left) and ANR (right). In the left group, energy bands $E(\mathbf{k})$ (left), density of states per area $\rho(E)$ (middle), and ballistic conductance $G_{\text{ballistic}}$ (right) are shown with their zoom-ins to the band edge for a ZNR with $N = 10$. In the right group, the same spectra with the same scales are plotted for an ANR with $N = 10$.

strong singularities in the entire spectrum, which are characteristic in Q1D structures. A distinguishing character of ρ in Q1D quartic materials from those of other materials is the emergence of excessively dense singularities at the MHS energy region (see Fig. 4). Both ANR and ZNR display rapid changes in their $G_{\text{ballistic}}$ close to the VBM (Fig. 4). In ZNR, top bands are more dispersive than in ANR, which is because of the narrower Brillouin zone of ANR. As a result, $G_{\text{ballistic}}$ values are larger for ZNR in these energies. Interestingly, we observe formation of nearly flat bands in ZNRs, close to the band edge. These nearly flat bands are formed by hybridization of quartic bands due to the edges. Flattening gives rise to even stronger peaks in the DOS.

It can be expected that the increase in the NR's width causes both the DOS and $G_{\text{ballistic}}$ spectra to evolve into those of the 2D system. Fig. 5 exhibits the evolution of $\rho(E)$ per area and $G_{\text{ballistic}}$ for different system widths, N , in the case of pristine ZNRs. Here, the corresponding 2D spectra are given by black curves. It can be observed in Fig. 5-top that, $\rho(E)$ approaches to that of 2D quartic system as N is systematically increased. Similarly, $G_{\text{ballistic}}$ of NRs approach to that of 2D quartic systems with increasing N , which is shown in the bottom panel of Fig. 5.

Width and edge-shape are determinant factors for the electronic structure and hence for the transport regimes. The effects of short-range Anderson disorder are studied for the Q1D systems for which the numerical calculations are performed for two different ribbon widths of $N = 10$ and $N = 20$ for both edge shapes. The evolution of conductance is examined for various device lengths at energies close to the VBM ($(E - E_{\text{VBM}})/t_1 \in [-0.12, 0]$) for a relatively weak realization of disorder ($W = 250$ meV). Length dependent G_{av} values of ZNR and ANR are plotted in Fig. 6(a). Although $G_{\text{ballistic}}$ values are close within this range, length dependent G_{av} decays much faster for the MHS energy region. This behavior is the same for both ANR and ZNR. The

origin of this behavior can be understood by examining the pristine DOS at these energies. As it is shown in Fig. 6(b-c), the pristine DOS (red cruves) has multiple singularities at the energies where G_{av} drops suddenly.

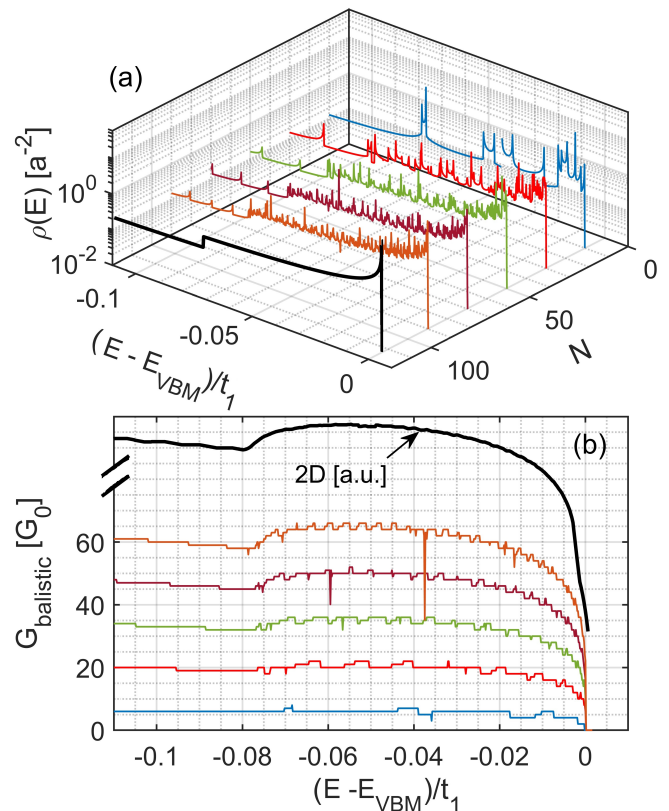


FIG. 5. Dependence of pristine DOS and conductance on ribbon width. DOS per area $\rho(E)$ (top) and $G_{\text{ballistic}}$ (bottom) for pristine ZNRs with $N = 10$ (blue), 30 (red), 50 (green), 70 (burgundy), and 90 (orange). For comparison, the corresponding 2D spectra are depicted with the black curves in each plot, and 2D $G_{\text{ballistic}}$ is given in arbitrary units.

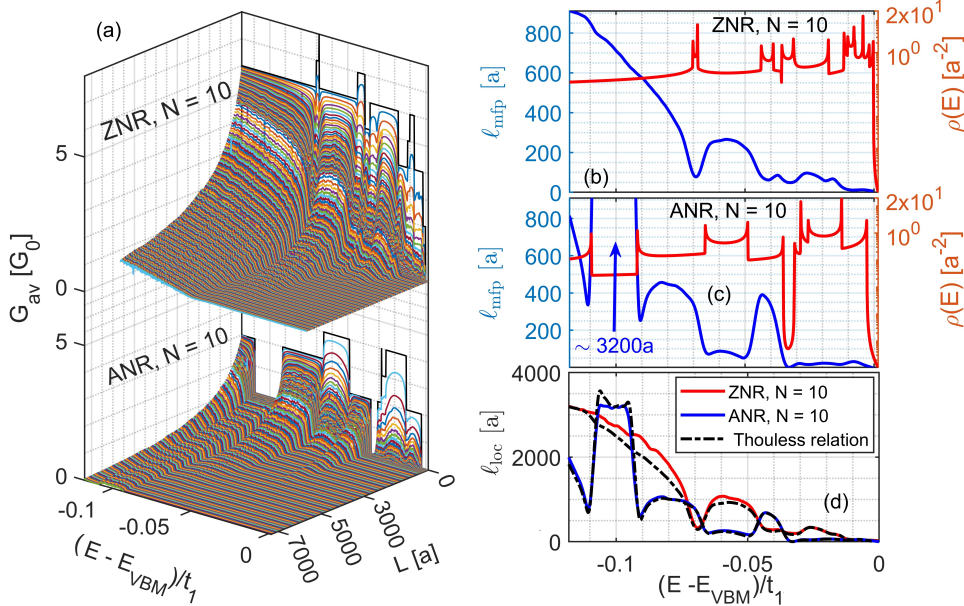


FIG. 6. Dependence of G_{av} on system length is shown in (a) for zigzag (top panel) and armchair (bottom panel) edge shapes with $N=10$. Disorder strength is $W=250$ meV. Mean-free-path (ℓ_{mfp}) (blue solid curves) and pristine DOS per unit area (red solid curves) are shown for ZNR and ANR in (b) and (c), respectively. In both cases, a family of strong singularities due to quartic dispersion are observed for $E > E_{VBM} - 0.07t_1$. The mean-free-path is much longer ($\ell_{mfp} \approx 3200a$) at energies away from the singularities. In panel (d), it is observed that the fitted localization length (ℓ_{loc} , red solid curve) is in a good agreement with that obtained from Thouless relation (dashed black curves).

The computed ℓ_{mfp} values are shown in the same plots (blue curves). We note that simulation data around $G_{ballistic}/2$ are used for fitting the diffusion formula, cf. Eq. 4. As it is expected, the dips in ℓ_{mfp} correspond to the peaks in the DOS, because higher the DOS it is much probable for the particle to scatter. In the MHS energy region, where the DOS values are high, ℓ_{mfp} of ZNR (ANR) always remains below $300a$ ($400a$). In the first conduction step, it is lower than $10a$ and at the band edge, ℓ_{mfp} converges to zero as $(E - E_{VBM})/t_1 \rightarrow 0$. On the contrast, $\ell_{mfp} \approx 3200a$ at energies outside the MHS energy region, namely for $(E - E_{VBM})/t_1 \sim -0.1$ for ANR.

The ℓ_{loc} values are obtained by fitting the G_{av} at $L \gg \ell_{mfp}$. The consistency of ℓ_{mfp} and ℓ_{loc} is checked by using Thouless relation (Eq. 5). Within the MHS energy region, the localization lengths are short and therefore they can be obtained within reasonable sizes of simulated devices. However, for lower energies this is not the case. Fig. 7(d) demonstrates ℓ_{loc} for the ZNR (red solid curve) and the ANR (blue solid curve) in which ℓ_{loc} approaches zero for both NRs as the energy goes to E_{VBM} . It is clear from Fig. 7(d) that for both NRs, Thouless relation (black dashed curves) are in good agreement with the fitted data, especially within the MHS energy region.

In order to reveal the effects of device width N on the transport length scales, the Q1D systems with $N = 10$ are compared to those with $N = 20$ for both edge shapes. Fig. 7(a) shows pristine DOS per area for the ZNRs with $N = 10$ (red solid curve) and $N = 20$ (blue solid curve) at the MHS energy region. The spectra explicitly display that $N = 20$ case has more singularities compared to the ZNR with $N = 10$ at the band edge. Multiple singularities exist around E_{VBM} for both sizes. Similarly, DOS for the ANR with $N = 10$ (pink solid curve) and $N = 20$ (yellow solid curve) are displayed in Fig. 7(d). It

is observed that the density of singularities increase with width. On the other hand, when the number of atoms in the unit cells are equal, the number of singularities in ZNRs is larger than in ANRs, simply because the number of bands within the MHS energy region is larger in ZNRs (see Fig. 4). Dense singularities in the DOS give rise to shorter ℓ_{mfp} independent of the edge termination.

In quasi-1D structures, system width affects ℓ_{mfp} by means of more than one mechanisms. First, considering the ribbon as dimensionally reduced form of the two-dimensional structure, edges are sources of scatterings, hence ℓ_{mfp} is expected to reduce with ribbon width. Indeed, it was reported that ℓ_{mfp} increases with width in edge disordered graphene nanoribbons [73, 74]. Similarly, in graphene NRs with oxygen functionalization, ℓ_{mfp} was shown to increase with the ribbon width [75]. However, in quartic NRs we do not observe such an increase in ℓ_{mfp} with width. On the contrary, ℓ_{mfp} can be greater for narrower ribbons at some energy values. This can be understood in terms of another factor that determines ℓ_{mfp} , namely the width dependence of DOS at MHS energy region. Recalling Fermi's golden rule, the scattering rate increases with the DOS, which is the reason of the dips in the computed ℓ_{mfp} (see Fig. 6(b-c) and Fig. 7(b,e)). In quartic NRs, the number of van Hove singularities depends on the ribbon width, namely narrower the ribbon, less the number of singularities. As a result, ℓ_{mfp} of wider ribbons are suppressed due to denser singularities. The trade-off between these two mechanisms is the main factor that determines width dependence of ℓ_{mfp} .

The localization length also depends on these factors. Additionally, the number of channels has an important role as it was described in Eq. 5. The number of channels increases with width, therefore unlike ℓ_{mfp} , ℓ_{loc} increases with width for both ANRs and ZNRs (Fig. 7(c,f)).

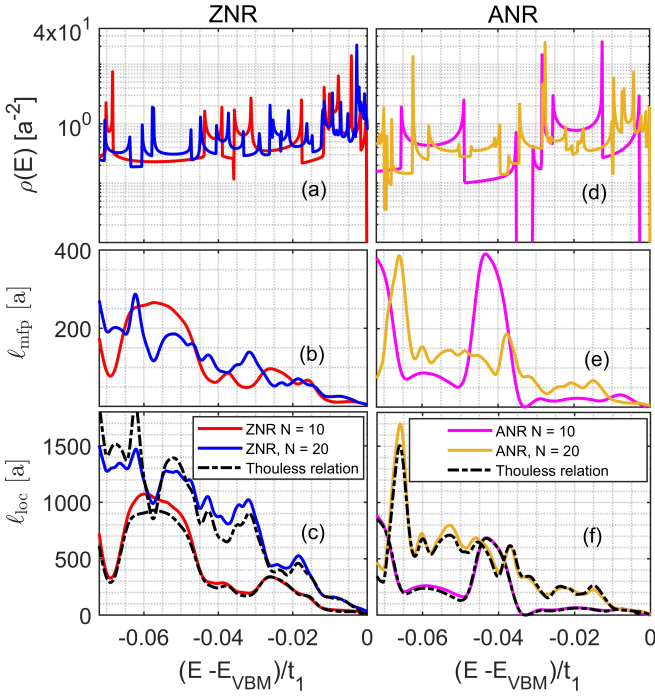


FIG. 7. Width dependence of DOS and transport length scales for both edge shapes. Pristine DOS per area for ZNRs with $N = 10$ (red) and $N = 20$ (blue) are plotted in (a). Corresponding mean-free-path (ℓ_{mfp}) (b) and localization lengths (ℓ_{loc}) is shown in (b) and (c). Black dashed curves exhibit the agreement in terms of Thouless relation. The same quantities are plotted for ANR with $N = 10$ (pink) and $N = 20$ (orange) in (d), (e), and (f).

Comparing ℓ_{loc} of ANRs and ZNRs, those of ZNRs are considerably longer, whereas their ℓ_{mfp} are similar. This difference is also rooted in the difference between the number of channels. ANRs have wider unit cells, and narrower Brillouin zones, therefore the quartic bands are less dispersive and the number of channels are less than ZNRs. Further details in the energy dependent ℓ_{loc} of quartic NRs can be understood by investigating the details in the DOS and $G_{\text{ballistic}}$.

C. Scaling Analysis

For analyzing the transport regimes in the limits of small and large L , the scaling function

$$\beta = \frac{d \ln G_{\text{av}}}{d \ln L} \quad (7)$$

of the one-parameter scaling theory [76–78] is used. In the case of disordered systems, the metal-insulator transition (MIT) can be studied through β as a function of $\ln(g)$, where the dimensionless conductance is $g = G_{\text{av}}/G_0$. There is a fixed point above (below) which the system scales towards a metal (an insulator) as the system size is increased. However, the system dimension

plays a crucial role in our conceptual understanding of MIT. The 2D system is the marginal case [77], but the systems with a dimension smaller than $d < 2$ undergo to the Anderson localization [76]. In addition, the Q1D quartic systems have the multiple strong singularities at the quartic band edge, pointing to the strong localization regime. For these reasons, we make use of the β -function to reveal the points where the diffusion regime ends and the localization regime starts. The two different forms of the β -function given below render easy to distinguish the transport regimes.

After some algebra, the β -function can be expressed in terms of corresponding length scales as

$$\beta = \begin{cases} -\frac{1}{1 + \frac{\ell_{\text{mfp}}}{L}} = \beta_{\text{dif}}, \\ -\frac{L}{\ell_{\text{loc}}} = \beta_{\text{loc}}. \end{cases} \quad (8)$$

The functions β_{dif} and β_{loc} depend on ℓ_{mfp} and ℓ_{loc} , which are to be extracted from fitting. It is also possible to investigate the scaling behavior directly from the simulation data without referring to any fitted parameter

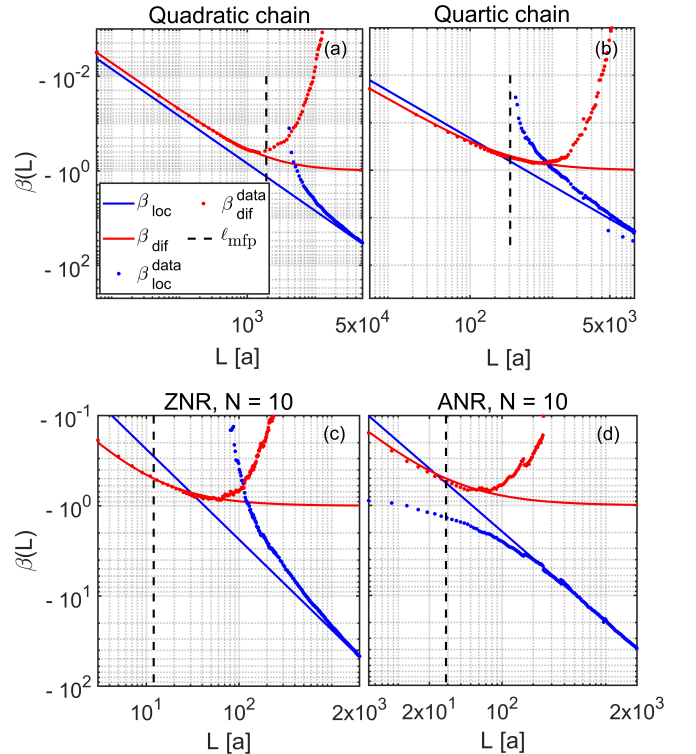


FIG. 8. Scaling function is used to distinguish transport regimes. In (a) and (b), the scaling functions are plotted for quadratic and quartic chains at $(E - E_{\text{VBM}})/t_1 = -0.017$. They are compared with data (cf. Eq. 8 and Eq. 9) Similar analysis is shown in (c) and (d) for ZNR and ANR, with $N = 10$, where energy is set to $(E - E_{\text{VBM}})/t_1 = -0.0023$.

as [79]

$$\beta^{\text{data}} = \begin{cases} \frac{G_{\text{av}}}{N_{\text{ch}}} - 1 = \beta_{\text{dif}}^{\text{data}}, \\ -\ln \frac{G_{\text{av}}}{\alpha} = \beta_{\text{loc}}^{\text{data}}. \end{cases} \quad (9)$$

Comparing β (Eq. 8) with β^{data} (Eq. 9) for the systems of interest, the transport regimes and their crossover are easy to distinguish. Moreover, the agreement between fitted transport length scales (ℓ_{mfp} and ℓ_{loc}) and the simulation data is possible to test.

In Fig. 8(a-b), we compare β with β^{data} for the strictly-1D systems, namely the quadratic and quartic chains, as functions of L for $(E - E_{\text{VBM}})/t_1 = -0.017$. The solid curves represent the β function (β_{dif} and β_{loc}), which are obtained using ℓ_{mfp} and ℓ_{loc} (which were obtained by fitting simulation data to Eq. 4). The data points represent β^{data} ($\beta_{\text{dif}}^{\text{data}}$ and $\beta_{\text{loc}}^{\text{data}}$), which do not rely on any fittings but are obtained solely from the simulation data. At short lengths, there is a perfect agreement between β_{dif} and $\beta_{\text{dif}}^{\text{data}}$ (Fig. 8(a-b), red curves and red dots). This also verifies that the ℓ_{mfp} fit is satisfactory. The ℓ_{mfp} values are indicated by vertical dashed curves ($\ell_{\text{mfp}} = 1903a$ for quadratic chain and $\ell_{\text{mfp}} = 308a$ for quartic chain). For $L > \ell_{\text{mfp}}$, the agreement between β_{dif} and $\beta_{\text{dif}}^{\text{data}}$ is lost. Namely, the simulation data do not obey the diffusion equation any more. This suggests that the fitting procedure for ℓ_{mfp} should use only the data from short distances (where $G_{\text{av}} \simeq G_{\text{ballistic}}/2$), as was done in this work. At long distances ($L \gg \ell_{\text{mfp}}$) we observe that the $\beta_{\text{loc}}^{\text{data}}$ converges to β_{loc} (blue curves and dots), which confirms that the fitted ℓ_{loc} is correct. We should note that the $\beta_{\text{loc}}^{\text{data}}$ converges to β_{loc} at distances longer than ℓ_{loc} . The intermediate distances where β^{data} is not in agreement with β_{dif} or β_{loc} are considered as the crossover region. The disagreement does not imply that ℓ_{mfp} or ℓ_{loc} are incorrect. The validity of ℓ_{loc} is confirmed by the fact that the slope of β_{loc} matches perfectly with $\beta_{\text{loc}}^{\text{data}}$ at long distances.

The same scaling analysis is performed for quartic

NRs as well. In Fig. 8(c-d), β and β^{data} are shown for ZNR($N=10$) and ANR($N=10$), respectively, at $(E - E_{\text{VBM}})/t_1 = -0.0023$. Transport length scales are found to be $\ell_{\text{mfp}} = 12a$ (28.8a) and $\ell_{\text{loc}} = 842.26a$ (51.43a) for the ZNR (ANR). As it was the case in strictly-1D systems, $\beta_{\text{dif}}^{\text{data}}$ is in very good agreement with β_{dif} at short L up to ℓ_{mfp} . At $L \ll \ell_{\text{mfp}}$, $\beta_{\text{loc}}^{\text{data}}$ converges to β_{loc} , showing that obtained ℓ_{loc} is consistent. We again observe that diffusion regime survives only at relatively short distances in quartic NRs. Although N_{ch} can be large, ℓ_{loc} is also relatively short because of multiple strong singularities close to the VBM. These findings are confirmed by the β -function analysis of simulation data, as well.

IV. CONCLUSION

In summary, a minimal TB model is combined with Landauer formalism, which is used for studying the transport properties of disordered quartic systems. The scaling theory is utilized in a way to distinguish the diffusion and localization regimes and to find the relevant length scales. A comparison of strictly-1D quartic chain against its quadratic counterpart at a given disorder strength, we show that ℓ_{mfp} and ℓ_{loc} of the quartic chain are much smaller in the MHS energy region. In quasi-1D quartic ribbons, ℓ_{mfp} and ℓ_{loc} are considerably short because of multiple strong van Hove singularities, which are denser and stronger in quartic systems compared to quadratic ones. Interestingly, ℓ_{mfp} can be longer in narrower NRs compared to the wider NRs, which is because the number of singularities increase with width in the MHS energy region.

ACKNOWLEDGMENTS

This work was supported by The Scientific and Technological Research Council of Turkey (TÜBİTAK) under 1001 Grant Project No. 119F353.

-
- [1] Kenneth S. Burch, David Mandrus, and Je-Geun Park. Magnetism in two-dimensional van der Waals materials. *Nature*, 563(7729):47–52, November 2018.
- [2] Salvador Barraza-Lopez, Benjamin M. Fregoso, John W. Villanova, Stuart S. P. Parkin, and Kai Chang. Colloquium: Physical properties of group-IV monochalcogenide monolayers. *Reviews of Modern Physics*, 93(1):011001, 2021.
- [3] Sheneve Z. Butler, Shawna M. Hollen, Linyou Cao, Yi Cui, Jay A. Gupta, Humberto R. Gutiérrez, Tony F. Heinz, Seung Sae Hong, Jiaying Huang, Ariel F. Ismach, Ezekiel Johnston-Halperin, Masaru Kuno, Vladimir V. Plashnitsa, Richard D. Robinson, Rodney S. Ruoff, Sayeef Salahuddin, Jie Shan, Li Shi, Michael G. Spencer, Mauricio Terrones, Wolfgang Windl, and Joshua E. Goldberger. Progress, Challenges, and Opportunities in Two-Dimensional Materials Beyond Graphene. *ACS Nano*, 7(4):2898–2926, April 2013.
- [4] Ganesh R. Bhimanapati, Zhong Lin, Vincent Meunier, Yeonwoong Jung, Judy Cha, Saptarshi Das, Di Xiao, Youngwoo Son, Michael S. Strano, Valentino R. Cooper, Liangbo Liang, Steven G. Louie, Emilie Ringe, Wu Zhou, Steve S. Kim, Rajesh R. Naik, Bobby G. Sumpter, Humberto Terrones, Fengnian Xia, Yeliang Wang, Jun Zhu, Deji Akinwande, Nasim Alem, Jon A. Schuller, Raymond E. Schaak, Mauricio Terrones, and Joshua A. Robinson. Recent Advances in Two-Dimensional Materials beyond Graphene. *ACS Nano*, 9(12):11509–11539, December 2015.

- [5] Karim Khan, Ayesha Khan Tareen, Muhammad Aslam, Renheng Wang, Yupeng Zhang, Asif Mahmood, Zhengbiao Ouyang, Han Zhang, and Zhongyi Guo. Recent developments in emerging two-dimensional materials and their applications. *Journal of Materials Chemistry C*, 8(2):387–440, 2020.
- [6] A. Avsar, H. Ochoa, F. Guinea, B. Ozyilmaz, B. J. van Wees, and I. J. Vera-Marun. *Colloquium*: Spintronics in graphene and other two-dimensional materials. *Reviews of Modern Physics*, 92(2):021003, June 2020.
- [7] Pere Miró, Martha Audiffred, and Thomas Heine. An atlas of two-dimensional materials. *Chemical Society Reviews*, 43(18):6537–6554, 2014.
- [8] Mingsheng Xu, Tao Liang, Minmin Shi, and Hongzheng Chen. Graphene-Like Two-Dimensional Materials. *Chemical Reviews*, 113(5):3766–3798, May 2013.
- [9] Tom Vincent, Jiayun Liang, Simrjit Singh, Eli G Castanon, Xiaotian Zhang, Amber McCreary, Deep Jariwala, Olga Kazakova, and Zakaria Y Al Balushi. Opportunities in electrically tunable 2d materials beyond graphene: Recent progress and future outlook. *Applied Physics Reviews*, 8(4):041320, 2021.
- [10] A. K. Geim and I. V. Grigorieva. Van der Waals heterostructures. *Nature*, 499(7459):419–425, July 2013.
- [11] Chunsen Liu, Huawei Chen, Shuiyuan Wang, Qi Liu, Yu-Gang Jiang, David Wei Zhang, Ming Liu, and Peng Zhou. Two-dimensional materials for next-generation computing technologies. *Nature Nanotechnology*, 15(7), 2020.
- [12] Mengqi Zeng, Yao Xiao, Jinxin Liu, Kena Yang, and Lei Fu. Exploring two-dimensional materials toward the next-generation circuits: from monomer design to assembly control. *Chemical reviews*, 118(13):6236–6296, 2018.
- [13] Zhen Zhu and David Tománek. Semiconducting layered blue phosphorus: a computational study. *Physical review letters*, 112(17):176802, 2014.
- [14] C Kamal and Motohiko Ezawa. Arsenene: Two-dimensional buckled and puckered honeycomb arsenic systems. *Physical Review B*, 91(8):085423, 2015.
- [15] O Üzengi Aktürk, V Ongun Özçelik, and S Ciraci. Single-layer crystalline phases of antimony: Antimonenes. *Physical review B*, 91(23):235446, 2015.
- [16] V Ongun Özçelik, O Üzengi Aktürk, Engin Durgun, and S Ciraci. Prediction of a two-dimensional crystalline structure of nitrogen atoms. *Physical Review B*, 92(12):125420, 2015.
- [17] Shengli Zhang, Zhong Yan, Yafei Li, Zhongfang Chen, and Haibo Zeng. Atomically thin arsenene and antimonene: semimetal-semiconductor and indirect-direct band-gap transitions. *Angewandte Chemie*, 127(10):3155–3158, 2015.
- [18] Jianping Ji, Xiufeng Song, Jizi Liu, Zhong Yan, Chengxue Huo, Shengli Zhang, Meng Su, Lei Liao, Wenhui Wang, Zhenhua Ni, et al. Two-dimensional antimonene single crystals grown by van der waals epitaxy. *Nature communications*, 7(1):1–9, 2016.
- [19] Shengli Zhang, Meiqiu Xie, Fengyu Li, Zhong Yan, Yafei Li, Erjun Kan, Wei Liu, Zhongfang Chen, and Haibo Zeng. Semiconducting group 15 monolayers: a broad range of band gaps and high carrier mobilities. *Angewandte Chemie*, 128(5):1698–1701, 2016.
- [20] E Aktürk, O Üzengi Aktürk, and S Ciraci. Single and bilayer bismuthene: Stability at high temperature and mechanical and electronic properties. *Physical Review B*, 94(1):014115, 2016.
- [21] Hâldun Sevinçli. Quartic dispersion, strong singularity, magnetic instability, and unique thermoelectric properties in two-dimensional hexagonal lattices of group-va elements. *Nano Letters*, 17(4):2589–2595, 2017.
- [22] Shengli Zhang, Shiyong Guo, Zhongfang Chen, Yeliang Wang, Hongjun Gao, Julio Gómez-Herrero, Pablo Ares, Félix Zamora, Zhen Zhu, and Haibo Zeng. Recent progress in 2d group-va semiconductors: from theory to experiment. *Chemical Society Reviews*, 47(3):982–1021, 2018.
- [23] R Bhuvaneswari, V Nagarajan, and R Chandiramouli. Recent advances in arsenene nanostructures towards prediction, properties, synthesis and applications. *Surfaces and Interfaces*, 28:101610, 2022.
- [24] Yaozhuang Nie, Mavlanjan Rahman, Pei Liu, Aihemaitijiang Sidike, Qinglin Xia, and Guang-hua Guo. Room-temperature half-metallicity in monolayer honeycomb structures of group-v binary compounds with carrier doping. *Physical Review B*, 96(7):075401, 2017.
- [25] Jun Zhao, Zheng-Hang Qi, Yong Xu, Jun Dai, Xiao Cheng Zeng, Wanlin Guo, and Jing Ma. Theoretical studies on tunable electronic structures and potential applications of two-dimensional arsenene-based materials. *Wiley Interdisciplinary Reviews: Computational Molecular Science*, 9(2):e1387, 2019.
- [26] Shiyong Guo, Wenhan Zhou, Bo Cai, Kan Zhang, Shengli Zhang, and Haibo Zeng. Band engineering realized by chemical combination in 2d group va–va materials. *Nanoscale Horizons*, 4(5):1145–1152, 2019.
- [27] Arnab Majumdar, Xiaoyong Yang, Wei Luo, Suman Chowdhury, Sudip Chakraborty, and Rajeev Ahuja. High exothermic dissociation in van der waals like hexagonal two dimensional nitrogene from first–principles molecular dynamics. *Applied Surface Science*, 529:146552, 2020.
- [28] Shengli Zhang, Hengze Qu, Jiang Cao, Yangyang Wang, Shengyuan A Yang, Wenhan Zhou, and Haibo Zeng. Extending channel scaling limit of p-mosfets through antimonene with heavy effective mass and high density of state. *IEEE Transactions on Electron Devices*, 69(2):857–862, 2022.
- [29] Houlong L Zhuang and Richard G Hennig. Single-layer group-iii monochalcogenide photocatalysts for water splitting. *Chemistry of Materials*, 25(15):3232–3238, 2013.
- [30] Xufan Li, Ming-Wei Lin, Alexander A Puzdov, Juan C Idrobo, Cheng Ma, Miaofang Chi, Mina Yoon, Christopher M Rouleau, Ivan I Kravchenko, David B Geohegan, et al. Controlled vapor phase growth of single crystalline, two-dimensional gase crystals with high photoresponse. *Scientific reports*, 4(1):1–9, 2014.
- [31] Ming-Wei Chen, HoKwon Kim, Dmitry Ovchinnikov, Agnieszka Kuc, Thomas Heine, Olivier Renault, and Andras Kis. Large-grain mbe-grown gase on gaas with a mexican hat-like valence band dispersion. *npj 2D Materials and Applications*, 2(1):1–7, 2018.
- [32] Huimin Wang, Guangzhao Qin, Jiayue Yang, Zhenzhen Qin, Yagang Yao, Qiang Wang, and Ming Hu. First-principles study of electronic, optical and thermal transport properties of group iii–vi monolayer mx (m=

- ga, in; $x = s, se$). *Journal of Applied Physics*, 125(24):245104, 2019.
- [33] Kai Xu, Lei Yin, Yun Huang, Tofik Ahmed Shifa, Junwei Chu, Feng Wang, Ruiqing Cheng, Zhenxing Wang, and Jun He. Synthesis, properties and applications of 2d layered m iii x vi ($m = ga, in; x = s, se, te$) materials. *Nanoscale*, 8(38):16802–16818, 2016.
- [34] Protik Das, Darshana Wickramaratne, Bishwajit Debnath, Gen Yin, and Roger K Lake. Charged impurity scattering in two-dimensional materials with ring-shaped valence bands: Gas, gase, ins, and inse. *Physical Review B*, 99(8):085409, 2019.
- [35] Mustafa Neşet Çınar, Gözde Özbal Sargin, Koray Sevim, Burak Özdamar, Gizem Kurt, and Hâldun Sevinçli. Ballistic thermoelectric transport properties of two-dimensional group iii-vi monolayers. *Physical Review B*, 103(16):165422, 2021.
- [36] Evgeny A Stepanov, Viktor Harkov, Malte Rösner, Alexander I Lichtenstein, Mikhail I Katsnelson, and Alexander N Rudenko. Coexisting charge density wave and ferromagnetic instabilities in monolayer inse. *npj Computational Materials*, 8(1):1–9, 2022.
- [37] Michael Ashton, Susan B Sinnott, and Richard G Hennig. Computational discovery and characterization of polymorphic two-dimensional iv–v materials. *Applied Physics Letters*, 109(19):192103, 2016.
- [38] Céline Barreteau, Baptiste Michon, Céline Besnard, and Enrico Giannini. High-pressure melt growth and transport properties of sip, sias, gep, and geas 2d layered semiconductors. *Journal of Crystal Growth*, 443:75–80, 2016.
- [39] Shengli Zhang, Shiyang Guo, Yaxin Huang, Zhen Zhu, Bo Cai, Meiqiu Xie, Wenhan Zhou, and Haibo Zeng. Two-dimensional sip: an unexplored direct band-gap semiconductor. *2D Materials*, 4(1):015030, 2016.
- [40] Ping Wu and Min Huang. Stability, bonding, and electronic properties of silicon and germanium arsenides. *physica status solidi (b)*, 253(5):862–867, 2016.
- [41] Fazel Shojaei and Hong Seok Kang. Electronic structures and li-diffusion properties of group iv–v layered materials: hexagonal germanium phosphide and germanium arsenide. *The Journal of Physical Chemistry C*, 120(41):23842–23850, 2016.
- [42] Ai-Qiang Cheng, Zi He, Jun Zhao, Hui Zeng, and Ru-Shan Chen. Monolayered silicon and germanium mononictide semiconductors: excellent stability, high absorbance, and strain engineering of electronic properties. *ACS applied materials & interfaces*, 10(6):5133–5139, 2018.
- [43] Liqin Zhou, Yu Guo, and Jijun Zhao. Geas and sias monolayers: Novel 2d semiconductors with suitable band structures. *Physica E: Low-dimensional Systems and Nanostructures*, 95:149–153, 2018.
- [44] Deobrat Singh, Shivam Kansara, Sanjeev K Gupta, and Yogesh Sonvane. Single layer of carbon phosphide as an efficient material for optoelectronic devices. *Journal of materials science*, 53(11):8314–8327, 2018.
- [45] Burak Özdamar, Gözde Özbal, M Neşet Çınar, Koray Sevim, Gizem Kurt, Birnur Kaya, and Hâldun Sevinçli. Structural, vibrational, and electronic properties of single-layer hexagonal crystals of group iv and v elements. *Physical Review B*, 98(4):045431, 2018.
- [46] S. Demirci, N. Avazlı, E. Durgun, and S. Cahangirov. Structural and electronic properties of monolayer group III monochalcogenides. *Physical Review B*, 95(11), March 2017.
- [47] Darshana Wickramaratne, Ferdows Zahid, and Roger K Lake. Electronic and thermoelectric properties of van der waals materials with ring-shaped valence bands. *Journal of Applied Physics*, 118(7):075101, 2015.
- [48] Agnieszka Kuc, Elias Cusati, Teresa akovsknd Dib, Augusto F Oliveira, Alessandro Fortunelli, Giuseppe Iannaccone, Thomas Heine, and Gianluca Fiori. High-performance 2d p-type transistors based on gase layers: An ab initio study. *Advanced Electronic Materials*, 3(2):1600399, 2017.
- [49] Ting Cao, Zhenglu Li, and Steven G Louie. Tunable magnetism and half-metallicity in hole-doped monolayer gase. *Physical review letters*, 114(23):236602, 2015.
- [50] Yandong Ma, Ying Dai, Meng Guo, Lin Yu, and Baibiao Huang. Tunable electronic and dielectric behavior of gas and gase monolayers. *Physical Chemistry Chemical Physics*, 15(19):7098–7105, 2013.
- [51] Dmitry V Rybkovskiy, Alexander V Osadchy, and Elena D Obratsova. Transition from parabolic to ring-shaped valence band maximum in few-layer gas, gase, and inse. *Physical Review B*, 90(23):235302, 2014.
- [52] Xiaochen Wang, Yuewen Sheng, Ren-Jie Chang, Ja Kyung Lee, Yingqiu Zhou, Sha Li, Tongxin Chen, Hefu Huang, Benjamin F. Porter, Harish Bhaskaran, and Jamie H. Warner. Chemical Vapor Deposition Growth of Two-Dimensional Monolayer Gallium Sulfide Crystals Using Hydrogen Reduction of Ga₂S₃. *ACS Omega*, 3(7):7897–7903, July 2018.
- [53] Sidong Lei, Liehui Ge, Zheng Liu, Sina Najmaei, Gang Shi, Ge You, Jun Lou, Robert Vajtai, and Pulickel M. Ajayan. Synthesis and Photoresponse of Large GaSe Atomic Layers. *Nano Letters*, 13(6):2777–2781, June 2013.
- [54] Chan Su Jung, Fazel Shojaei, Kidong Park, Jin Young Oh, Hyung Soon Im, Dong Myung Jang, Jeunghee Park, and Hong Seok Kang. Red-to-Ultraviolet Emission Tuning of Two-Dimensional Gallium Sulfide/Selenide. *ACS Nano*, 9(10):9585–9593, October 2015.
- [55] Fucui Liu, Hidekazu Shimotani, Hui Shang, Thangavel Kanagasekaran, Viktor Zólyomi, Neil Drummond, Vladimir I. Fal’ko, and Katsumi Tanigaki. High-Sensitivity Photodetectors Based on Multilayer GaTe Flakes. *ACS Nano*, 8(1):752–760, January 2014.
- [56] Xufan Li, Ming-Wei Lin, Alexander A Puzos, Juan C Idrobo, Cheng Ma, Miaofang Chi, Mina Yoon, Christopher M Rouleau, Ivan I Kravchenko, David B Geohegan, et al. Controlled vapor phase growth of single crystalline, two-dimensional gase crystals with high photoresponse. *Scientific reports*, 4(1):1–9, 2014.
- [57] PingAn Hu, Lifeng Wang, Mina Yoon, Jia Zhang, Wei Feng, Xiaona Wang, Zhenzhong Wen, Juan Carlos Idrobo, Yoshiyuki Miyamoto, David B Geohegan, et al. Highly responsive ultrathin gas nanosheet photodetectors on rigid and flexible substrates. *Nano letters*, 13(4):1649–1654, 2013.
- [58] Sidong Lei, Fangfang Wen, Liehui Ge, Sina Najmaei, Antony George, Yongji Gong, Weilu Gao, Zehua Jin, Bo Li, Jun Lou, Junichiro Kono, Robert Vajtai, Pulickel Ajayan, and Naomi J. Halas. An Atomically Layered InSe Avalanche Photodetector. *Nano Letters*, 15(5):3048–

- 3055, May 2015.
- [59] Denis A. Bandurin, Anastasia V. Tyurnina, Geliang L. Yu, Artem Mishchenko, Viktor Zólyomi, Sergey V. Morozov, Roshan Krishna Kumar, Roman V. Gorbachev, Zakhar R. Kudrynskiy, Sergio Pezzini, Zakhar D. Kovalyuk, Uli Zeitler, Konstantin S. Novoselov, Amalia Patané, Laurence Eaves, Irina V. Grigorieva, Vladimir I. Fal'ko, Andre K. Geim, and Yang Cao. High electron mobility, quantum Hall effect and anomalous optical response in atomically thin InSe. *Nature Nanotechnology*, 12(3):223–227, March 2017.
- [60] Jiadong Zhou, Jia Shi, Qingsheng Zeng, Yu Chen, Lin Niu, Fucui Liu, Ting Yu, Kazu Suenaga, Xinfeng Liu, Junhao Lin, and Zheng Liu. InSe monolayer: synthesis, structure and ultra-high second-harmonic generation. *2D Materials*, 5(2):025019, March 2018.
- [61] Wei Zhang, Hanna Enriquez, Yongfeng Tong, Azzedine Bendounan, Abdelkader Kara, Ari P. Seitsonen, Andrew J. Mayne, Gérald Dujardin, and Hamid Oughaddou. Epitaxial Synthesis of Blue Phosphorene. *Small*, 14(51):1804066, 2018.
- [62] Heping Li, Dechun Zhou, Qingyuan He, Nan Si, Benwu Xin, Saiyu Bu, Qingmin Ji, Hui Li, Harald Fuchs, and Tianchao Niu. Experimental Realization and Phase Engineering of a Two-Dimensional SnSb Binary Honeycomb Lattice. *ACS Nano*, 15(10):16335–16343, October 2021.
- [63] P. R. Wallace. The band theory of graphite. *Phys. Rev.*, 71:622–634, May 1947.
- [64] Supriyo Datta. *Electronic transport in mesoscopic systems*. Cambridge university press, 1997.
- [65] Dmitry Ryndyk. *Theory of Quantum Transport at Nanoscale: An Introduction*. Springer, December 2015.
- [66] MP Lopez Sancho, JM Lopez Sancho, JM Lopez Sancho, and J Rubio. Highly convergent schemes for the calculation of bulk and surface green functions. *Journal of Physics F: Metal Physics*, 15(4):851, 1985.
- [67] Norbert Nemeč and Gianuario Cuniberti. Hofstadter butterflies of carbon nanotubes: Pseudofractality of the magnetoelectronic spectrum. *Physical Review B*, 74(16):165411, 2006.
- [68] Philip W Anderson, DJ Thouless, E Abrahams, and DS Fisher. New method for a scaling theory of localization. *Physical Review B*, 22(8):3519, 1980.
- [69] J Sak and B Kramer. Transmission of particles through a random one-dimensional potential. *Physical Review B*, 24(4):1761, 1981.
- [70] KS Chase and A MacKinnon. The statistics of the conductance in two-and three-dimensional disordered systems. *Journal of Physics C: Solid State Physics*, 20(36):6189, 1987.
- [71] Carlo WJ Beenakker. Random-matrix theory of quantum transport. *Reviews of modern physics*, 69(3):731, 1997.
- [72] Philip W Anderson. Absence of diffusion in certain random lattices. *Physical review*, 109(5):1492, 1958.
- [73] Denis A Areshkin, Daniel Gunlycke, and Carter T White. Ballistic transport in graphene nanostrips in the presence of disorder: importance of edge effects. *Nano letters*, 7(1):204–210, 2007.
- [74] Aurélien Lherbier, Blanca Biel, Yann-Michel Niquet, and Stephan Roche. Transport length scales in disordered graphene-based materials: strong localization regimes and dimensionality effects. *Physical review letters*, 100(3):036803, 2008.
- [75] Alessandro Cresti, Alejandro Lopez-Bezanilla, Pablo Ordejón, and Stephan Roche. Oxygen Surface Functionalization of Graphene Nanoribbons for Transport Gap Engineering. *ACS Nano*, 5(11):9271–9277, 2011.
- [76] Elihu Abrahams, PW Anderson, DC Licciardello, and TV Ramakrishnan. Scaling theory of localization: Absence of quantum diffusion in two dimensions. *Physical Review Letters*, 42(10):673, 1979.
- [77] Patrick A Lee and TV Ramakrishnan. Disordered electronic systems. *Reviews of modern physics*, 57(2):287, 1985.
- [78] Yoseph Imry. *Introduction to Mesoscopic Physics*. Oxford University Press, 2002.
- [79] Mustafa Neşet Çımar, Aleandro Antidormi, Viet-Hung Nguyen, Alessandro Kovtun, Samuel Lara-Avila, Andrea Liscio, Jean-Christophe Charlier, Stephan Roche, and Hâldun Sevinçli. Toward optimized charge transport in multilayer reduced graphene oxides. *Nano letters*, 22(6):2202–2208, 2022.